Article

The Effects of a Seagull Airfoil on the Aerodynamic Performance of a Small Wind Turbine

Dean Sesalim * and Jamal Naser *

Department of Mechanical and Product Design Engineering, Swinburne University of Technology, Hawthorn, VIC 3122, Australia
* Correspondence: dsesalim@swin.edu.au (D.S.); jnaser@swin.edu.au (J.N.)

Abstract: Birds' flight characteristics such as gliding and dynamic soaring have inspired various optimizations and designs of wind turbines. The implementation of biological wing geometries such as the airfoil profile of seabirds has improved wind turbine performance. However, the field can still benefit from further investigation into the aerodynamic characteristics of an inspired design. Therefore, this study evaluated the effect of a seagull airfoil design on the aerodynamic performance of the National Renewable Energy Laboratory (NREL) Phase VI wind turbine. By replacing its S809 airfoil with the laser-scanned profile of the seagull airfoil, the aerodynamic behavior at key locations of the NREL Phase VI wind turbine blade was numerically simulated in a three-dimensional environment using the Ansys Fluent 2022 R1 computational fluid dynamics (CFD) code. The results were validated against the experimental data, and analysis of the torque outputs, pressure distributions, and velocity profiles that were generated by both the baseline and modified models demonstrated the ability of the seagull airfoil profile to modify regions of minimum and maximum local velocities to achieve highly favorable pressure differentials, significantly increasing the torque output of the NREL Phase VI wind turbine by 350, 539, 823, and 577 Nm at 10, 15, 20, and 25 m/s inlet velocities, respectively.

Keywords: wind turbine performance; airfoil design; biological inspiration; wind turbine simulation

1. Introduction

The aerodynamic fundamentals of sustained bird flight correspond to the operation of lift-based wind turbines, in which lift is generated by air flowing over the wing, and the drag force opposing the direction of motion causes a loss of energy. In general, the shape of a wing determines a bird's flight characteristics and performance through trade-offs between speed, maneuverability, and efficiency. High-speed, high-lifting, elliptical, and soaring are the four types of wings that are adapted to specific environments and needs [1,2]. High-speed wings are short with pointed tips, enabling birds such as the swallow and falcon to reach powered flight speeds of 65 and 170 km/h, respectively [3,4]. High-lifting wings, on the other hand, allow for better take-off, but their low aspect ratio subjects them to high induced drag. However, the slots at the tip of high-lifting wings reduce drag by allowing the higher-pressure flow of the lower surface at the tip to be captured, hence reducing the wingtip vortices [5]. The characteristics most relevant to the operation of wind turbines, however, are those of soaring wings. Here, the high aspect ratio and low wing loading of soaring wings empower gliding flight and dynamic soaring, taking advantage of wind speed variation to generate lift. This allows birds such as seabirds, nightjars, and kestrels to fly slowly and almost hover in slight winds. While wings with an elliptical shape allow birds such as tyrant flycatchers to perform tight maneuvers, some high-aspect-ratio wings, such as those of the albatross, have nearly elliptical shapes with small-radius tips. This allows albatrosses to combine soaring techniques and efficient long-distance travel with substantial maneuverability [6–8].

Moreover, the conditions in which albatrosses fly closely resemble the conditions in which wind turbines in general, and small wind turbines (SWTs) in particular, usually

operate to extract wind energy. Under continuous changes in airflow speed and direction, a problem arises for a small wind turbine operating outside the design speed when the relative velocity becomes too high. And as the relative wind velocity increases, so does the angle of attack (AoA), creating drag and resulting in less generated lift due to the separation of flow. This results in a decreasing lift-to-drag ratio for a given airfoil design [9]. Therefore, the NREL developed the S-series airfoil design to reduce the performance losses of wind turbines with stall control [10]. However, this development relies on effective stall regulation in the turbine's blades and, thus, is not a practical solution in the case of SWTs due to the resulting cost and risk of failure.

Meanwhile, the development of SWT blades has recently benefited from bioinspired airfoil design in general [11], in particular seagull airfoils [12,13]. Although albatrosses have a significantly larger wingspan than seagulls, they also share a very similar airfoil cross-section and attributes. In fact, the more agile flight characteristics of seagulls seem better suited for the operations of SWTs. A study published in 2016 compared pressure distributions over an airfoil design based on a seagull wing to those over the high-lift, low-Reynolds-number S1223 airfoil at an AoA of 0 and 5°, finding that the pressure around the seagull airfoil was the least affected by the change in AoA despite the very similar geometrical properties that these two airfoils share [14]. While this gives an indication of the reason why the design of the seagull airfoil provides better performance for SWTs, an in-depth investigation into the reason(s) behind such versatility in operation is yet to be undertaken. Therefore, this work aims to evaluate the effects of the seagull airfoil design on the aerodynamic characteristics of an SWT by replacing the airfoil section of an SWT baseline model with an airfoil of a seagull.

2. Methodology

Using high-resolution three-dimensional CFD analysis of realistically rotating turbine blades with closely matched geometrical representations and dynamic conditions of the baseline model, this analysis aimed to provide reliable and accurate numerical predictions of aerodynamic quantities. To ensure this, the CFD results of the baseline model were validated using the NREL Phase VI experimental data. The NREL Phase VI experiment provided necessary data for validating the numerical analysis of wind turbines [15–19]. The use of the NREL Phase VI wind turbine as a baseline model in this analysis also ensured a valid comparison between the original and optimized performances.

Valid optimization results were also ensured by employing the seagull airfoil profile provided by the study published in 2016 [14]. This seagull airfoil was generated by averaging the cross-sections along the span of the wing of a seagull. Three-dimensional laser scanning was used with an accuracy of 0.041 mm. A semi-automated web-based tool was used to specify the airfoil coordinates on the image of the seagull airfoil published by the work [20]. This tool implements algorithms to allocate data points to extract the X and Y coordinates listed in Table 1. Afterward, the data were transferred to an Excel file and imported by the Autodesk Inventor 2023 parametric modeler to create the airfoil shown in Figure 1.

Figure 1. Cross-section of the modeled seagull airfoil.

Table 1. Seagull airfoil coordinate points.

Upper Surface		Lower Surface	
x/c		x/c	
y/c		y/c	
1		0	
0.92993		0.031035	
0.7997		0.070418	
0.66972		0.098108	
0.6155		0.1068	
0.5633		0.11494	
0.50037		0.123	
0.42815		0.129	
0.37163		0.13169	
0.30726		0.133	
0.2563		0.12993	
0.19		0.12	
0.13778		0.10657	
0.11539		0.0985	
0.099293		0.090545	
0.084438		0.08282	
0.070202		0.075298	
0.05968		0.068284	
0.047301		0.060253	
0.036159		0.052121	
0.027494		0.045717	
0.018829		0.037076	
0.011401		0.028537	
0.0044444		0.018978	
0		0	
0.0023234		−0.0064312	
0.01037		−0.013139	
0.025185		−0.016058	
0.08		−0.013	
0.13767		−0.0038977	
0.17687		0.004	
0.2257		0.013222	
0.3085		0.027596	
0.36489		0.035043	
0.4261		0.040955	
0.49047		0.045365	
0.55419		0.046196	
0.61921		0.045693	
0.68358		0.042362	
0.74177		0.037599	
0.8633		0.023534	
1		0	

2.1. Geometry and Conditions

The NREL Phase VI experimental wind turbine is a two-blade small horizontal axis wind turbine with a 10.058 m rotor diameter and a hub height of 12.192 m [21]. The blades were formed using the S809 airfoil profile and consist of 26 sections of various twist angles and chord lengths as listed in Table 2. The resulting main dimensions at key span locations of the modeled blade are shown in Figure 2.

Table 2. Blade parameters [21].

| Radial Distance R (m)	Span Station (R/5.029)	Chord Length (m)	Twist (Degrees)	Thickness (m) (20.95% Chord)	Twist Axis (% Chord), (m)
0.0	0.0	Hub center of rotation	Hub center of rotation	Hub center of rotation	Hub center of rotation
0.508	0.101	218 (root hub adapter)	0.0 (root hub adapter)	0.218 (root hub adapter)	50 (root hub adapter)
0.660	0.131	0.218	0.0	0.218	50
0.883	0.176	0.183	0.0	0.183	50
1.257	0.250	0.737	20.040	0.154	30, (0.221)
1.343	0.267	0.728	18.074	0.152	30, (0.218)
1.510	0.300	0.711	14.292	0.149	30, (0.213)
1.648	0.328	0.697	11.909	0.146	30, (0.209)
1.952	0.388	0.666	7.979	0.139	30, (0.199)
2.257	0.449	0.636	5.308	0.133	30, (0.190)
2.343	0.466	0.627	4.715	0.131	30, (0.188)
2.562	0.509	0.605	3.425	0.126	30, (0.181)
2.867	0.570	0.574	2.083	0.120	30, (0.172)
3.172	0.631	0.543	1.150	0.113	30, (0.162)
3.185	0.633	0.542	1.115	0.113	30, (0.162)
3.476	0.691	0.512	0.494	0.107	30, (0.153)
3.781	0.752	0.482	−0.015	0.100	30, (0.144)
4.023	0.800	0.457	−0.381	0.095	30, (0.137)
4.086	0.812	0.451	−0.475	0.094	30, (0.135)
4.391	0.873	0.420	−0.920	0.088	30, (0.162)
4.696	0.934	0.389	−1.352	0.081	30, (0.116)
4.780	0.950	0.381	−1.469	0.079	30, (0.114)
5.000	0.994	0.358	−1.775	0.075	30, (0.107)
5.029	1	0.335	−1.944	0.075	30, (0.101)
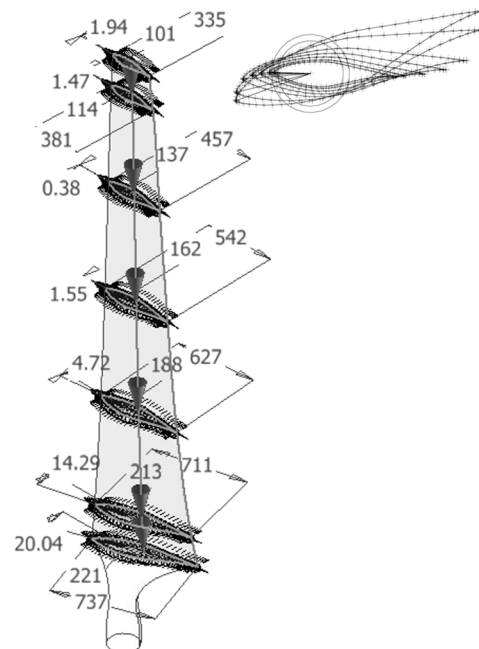
Figure 2. Cambers and twist distribution of the modeled blade.

Sequence S of the experiment consisted of the least complex conditions with rigid upwind configurations and no blade tip attachment. The blades were unteetered, and the tilt, yaw, and cone angles were maintained at 0° with a negligible decrease in rotor diameter due to the flapping during operation; quantization errors were limited to 0.024%. Moreover, no significant aerodynamic impact from the tower or the hub was reported.

The configuration was further simplified by maintaining a blade tip pitch angle of 3°, inlet speeds of 5, 10, 15, 20, and 25 m/s uniformly, and a constant rotation velocity of approximately 72 RPM (71.63 RPM synchronous velocity). Therefore, the conditions resemble steady flow conditions, and thus, this analysis assumes steady-state simulation. The interaction of solid surfaces in the flow volume was also eliminated since the analysis is concerned with the aerodynamic behavior of the turbine and not its structure. Generally, a sufficiently large computational domain is required to capture the flow characteristics and achieve correct results [22–26]. However, this depends on different factors such as the type of CFD code, its reliance, the turbulence model, and the meshing strategy. Nevertheless, the test section where the NREL Phase VI wind turbine was tested is already large, measuring 24.4 m high, 36.6 m wide, and 57.912 m long [27]. The default 1.225 kg/m^3 density at sea level, 101,325 Pa static pressure, and no-slip boundary conditions are used to capture the thin boundary layers on the walls, including those of the wind tunnel. Figure 3 describes the steps of the simulation.
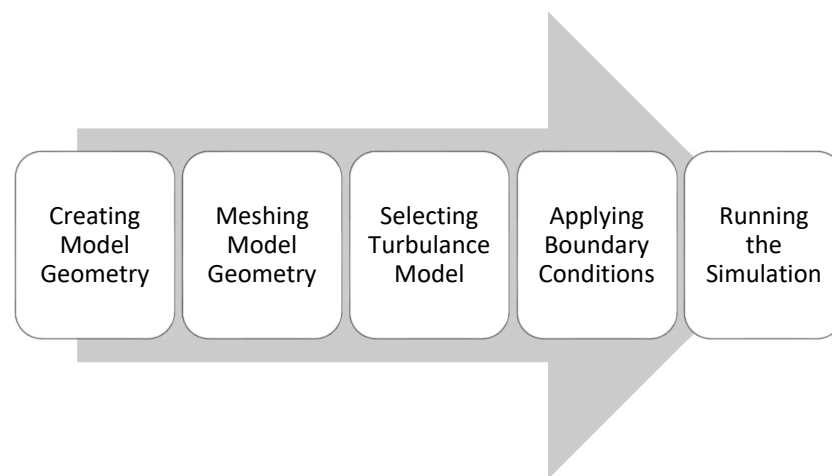

Figure 3. Simulation steps.

2.2. Turbulence Model

Modern CFD codes such as Ansys Fluent provide several turbulence models suitable for the aerodynamic analysis of rotating systems. But by default, the Shear Stress Transport (SST) $k - \omega$ model is selected in Ansys Fluent for the analysis of wind turbines. Name selections of surfaces and volumes help the program identify them. The general advantage of the SST $k - \omega$ model in the case of wind turbines is its ability to model flow behavior near the surfaces of the blades as well as in the far freestream with efficiency by gradually switching between the $k - \omega$ and the $k - \varepsilon$ turbulence models. This overcomes the limitation of the $k - \omega$ model in correctly modeling turbulence far from the surfaces and the $k - \varepsilon$ near the surface. The result is reliable accuracy with reasonable computational cost. The SST $k - \omega$ model is also effective in simulating turbulences created by the low-Reynolds-number NREL Phase VI wind turbine since the turbulent viscosity is eased by a coefficient in the transport equations used to obtain the model. Here, the reduction coefficient is given by

$$\alpha^* = \alpha^*_\infty \left(\frac{\alpha^*_0 + \frac{Re_t}{R_k}}{1 + \frac{Re_t}{R_k}} \right) \tag{1}$$

where $R_k = 6$ and

$$Re_t = \frac{\rho k}{\mu \omega} \tag{2}$$

And

$$\alpha^*_0 = \frac{\beta_i}{3} \tag{3}$$

where $\beta_i = 0.072$.

The reduction coefficient is implemented in the generation of ω through a standard coefficient given by

$$\alpha = \frac{\alpha_\infty}{\alpha^*}\left(\frac{\alpha_0 + \frac{Re_t}{R_\omega}}{1 + \frac{Re_t}{R_\omega}}\right) \tag{4}$$

where $R_\omega = 2.95$ and the generation of ω is given by

$$G_\omega = \alpha\frac{\omega}{k}G_k \tag{5}$$

where the generation of k is given by

$$G_k = -\rho\overline{u_j^i u_j^i}\frac{\partial u_j}{\partial x_i} \tag{6}$$

Finally, the approximate forms of governing equations are given by

$$\frac{\partial}{\partial t}(\rho\omega) + \frac{\partial}{\partial x_i}(\rho\omega u_i) = \frac{\partial}{\partial x_j}\left(\Gamma_\omega\frac{\partial\omega}{\partial x_j}\right) + G_\omega - Y_\omega \tag{7}$$

and

$$\frac{\partial}{\partial x}(\rho k) + \frac{\partial}{\partial x_i}(\rho k u_i) = \frac{\partial}{\partial x_j}\left(\Gamma_k\frac{\partial k}{\partial x_j}\right) + G_k - Y_k \tag{8}$$

This results in a considerable reduction in the propagation of low-Reynolds-number effects with the increase in velocity due to the high viscosity associated with low Reynolds numbers.

2.3. Meshing Strategy

Given the need to capture the geometrical details of the airfoil sections in this analysis, higher mesh resolution is necessary in areas of gradients such as surfaces with curvatures in order to capture the geometrical effects and enhanced calculation in regions of pressure for the purpose of comparison, not by increasing the overall mesh resolution, but by aiming the refinement in regions of interest. Therefore, control of the Curvature Normal Angle and the Curvature Min Size in ANSYS Mesh 2022 R1 is relied on to achieve localized refinement in regions with rapid size change. As a result, most of the mesh resolution accumulated on the surfaces of the blades where the higher the gradient, the higher the resolution, while no curvature regions remained unaffected by the refinement.

Meanwhile, a Y+ value of less than 2 was found appropriate for the accurateness of the NREL Phase VI wind turbine boundary layer thickness prediction when using tetrahedral cells [28]. But to decrease computational cost further, tetrahedral cells are transformed into polyhedral cells by the ANSYS Fluent 2022 R1 as illustrated in Figure 4 in order to reduce the number of cells while maintaining high resolution. This is because the higher number of nodes of each polyhedral cell allows for more bordering cells to better approximate the gradient with fewer cells. The default Y+ value of 1 is therefore used. Near-wall treatment of hexahedral mesh cells was found to be effective at capturing the flow characteristics in the boundary layer since it augments the mesh to create a better transition across the surface and ensure uniformity in the cell height throughout the transition.

The predicted torque results in Figure 5 using three sets of differing mesh resolutions for the 10 m/s inlet velocity case achieves mesh independency with the intermediate resolution since the higher mesh did not produce results enhancement of more than 5% towards the measured torque. The three resolutions are based on Curvature Minimum Sizes of 3, 2, and 1 mm and Curvature Minimum Angles of 3, 2, and 1 degrees using the ANSYS Fluent default -1000 minimum residual convergence criterion.
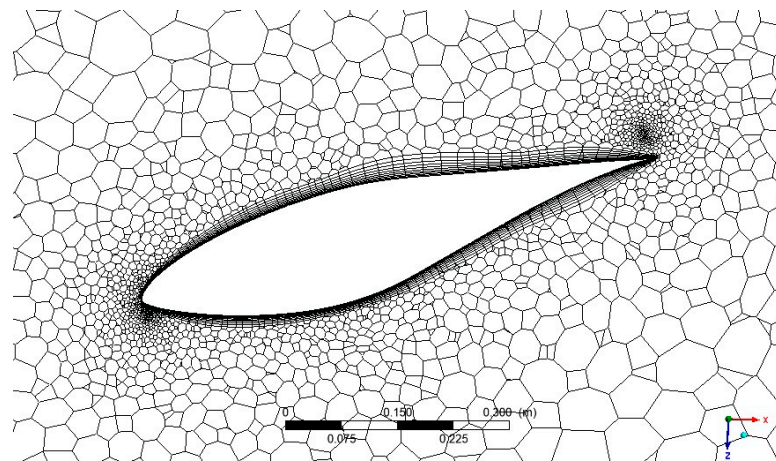
Figure 4. Cross-section view of the S809 airfoil surface meshing.
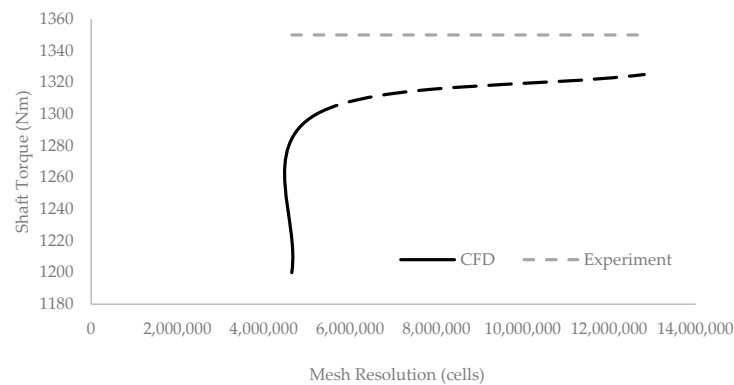

Figure 5. Mesh sensitivity study.

3. Results and Discussion

With the seagull airfoil implemented in the baseline model at matched parameters for each of the span locations as listed in Table 2, the performance characteristics of the modified model are discussed and evaluated in comparison to those of the baseline model. The comparison is also conducted with the exact same NREL Phase VI Sequence S test parameters as the baseline model's boundary conditions, and the numerical outputs of the baseline model are verified against the experimental data.

3.1. Torque Outputs

At first glance, the resulting torque outputs from the modified model shown in Figure 6 confirm the ability of the seagull airfoil profile to improve the performance of an SWT model. Here, the numerical torque results of the baseline model, which are in close agreement with the measured results as illustrated by the figure, are significantly enhanced by the seagull airfoil design despite no optimization of parameters such as the cord length and the twist distribution. Although both models experience drops in performance immediately after the 10 m/s inlet velocity, the recovery by the modified model is at the 15 m/s inlet velocity as opposed to the 20 m/s inlet velocity at which the baseline model has recovered. Here, the model generated 1254 Nm at the 10 m/s inlet velocity, while the modified model generated 1604 Nm at the same velocity. The variations in the generated torque at the 15 m/s inlet velocity from both models are nearly proportional, but opposite, as the modified model increased its generated torque to 1721 Nm while the baseline model decreased its generated torque to 1182 Nm at this velocity. Furthermore, the modified model was advanced by its much higher performance at the 10 m/s inlet velocity. This has contributed to the increase in its torque output as the inlet velocity increased. Also, the rise in torque output by the

modified model seems to be steady, improving by approximately 300 Nm for each 5 m/s increase in inlet velocity. This is while the performance of the baseline model fluctuated considerably, from a slight decrease to 1163 Nm at the 20 m/s inlet velocity to a sudden increase to 1539 Nm at the 25 m/s inlet velocity. The performance of the seagull airfoil is therefore more suitable for the operation of SWTs.
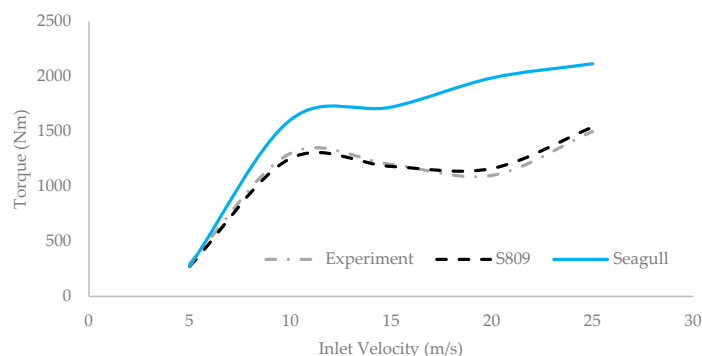

Figure 6. Torque results and comparison.

However, the significantly higher performance results of the modified model seem to challenge the Betz limit. Fundamentally, the shape of the power curve is influenced by the possible maximum power occurring at 59.3% of the dynamic power according to the Betz limit [29]. Here, the limit is defined as

$$C_P = 4a(1-a)^2 \tag{9}$$

where the axial induction factor a is defined as

$$a = \frac{V_1 - V_2}{V_1} \tag{10}$$

where V_1 and V_2 are the upstream and near rotor wind velocities, respectively. The optimum axial induction factor is therefore used to find the maximum coefficient of power, and the wind turbine cannot extract all the energy because the axial induction factor drops below the optimal value [29,30] p. 65. Physicist Albert Betz, however, defined a wind turbine as an open, two-dimensional actuator disk through which energy is taken from flow by the conservation of mass despite the induced drags. Therefore, reducing the drag penalty on the power output could be the effect of the seagull airfoil design on the baseline model. However, a theoretical drag-free optimal airfoil design is not possible. This raises the question of why the analytical results suggested that the nonoptimized seagull airfoil significantly outperformed the S809 airfoil which was optimized for the operation of the NREL Phase VI wind turbine model. To answer this question, an in-depth analysis of the aerodynamic characteristics of both models is necessary.

3.2. Pressure Distributions

The pressure around an airfoil helps evaluate the produced lift. This is because aerodynamic coefficients such as the coefficient of lift are integrals of the pressure coefficient curve along the chord of a two-dimensional airfoil section. Here, the relative pressure is defined, regardless of size, by the dimensionless pressure coefficient at the pertinent location in the flow field close to the surface. This aids in identifying the crucial areas where the forces of the flow molecules are mostly active. To capture the most active regions of pressure distributions, each of the NREL Phase VI wind turbine blades was fitted with pressure taps at the 30%, 46.6%, 63.3%, 80%, and 95% span locations [21]. Therefore, the two-dimensional pressure distributions around those span locations are analyzed and compared for both the baseline and the modified model to help verify the accuracy of the torque results, identify stall conditions, and investigate the causes for the calculated

torque results for the inlet velocity cases where the results for both models have varied considerably. This excludes the 5 m/s inlet velocity case where the torque values produced by both models are similar. To calculate the pressure coefficient values, an expression is added to ANSYS CFD Post resampling the following pressure coefficient formula:

$$C_p = \frac{\left(P - P_{ref}\right)}{q_{ref}} = \frac{(P - P_\infty)}{\left(\frac{1}{2}\rho V_\infty^2\right)} \tag{11}$$

where the following definitions hold:

P is the static pressure;

P_{ref} is the reference pressure;

q_{ref} is the reference dynamic pressure;

P_∞ is the freestream static pressure;

ρ is the flow density;

V_∞ is the relative velocity.

The numerical results of the baseline model are also validated against the measured values in Figures 7–10.

The figures also reveal much higher lift forces acting on the seagull airfoil and contributing to the torque results for the modified model. This lift is represented by large pressure differentials in favor of the lifting surface created using the seagull airfoil in comparison to the pressure around that created using the S809 airfoil. Furthermore, the pressures generated by the lifting surfaces of the blade implementing the seagull airfoil have gradually decreased as the inlet velocity increased, ranging from approximately $-4\,C_p$ at the 10 m/s inlet velocity to almost $-14\,C_p$ at the 25 m/s inlet velocity. This increase in lifting force is also considerable at the 15 m/s inlet velocity, which explains the earlier stall recovery by the modified model in comparison to the delayed recovery by the baseline model at the later 20 m/s inlet velocity. However, the pressure differentials generated by the modified blade have increased during all the inlet velocities as the relative velocity increased along the span of the blade. This is not the case for the baseline model as the near-symmetrical shape of the S809 airfoil has considerably reduced the velocity effects along the span of the blade, particularly at the tip, reducing the reduce the resulting pressure drag. Nevertheless, the pressure generated by the lifting surface of the baseline model remained considerably higher than that generated by the lifting surface of the modified model. In fact, the minimum pressure generated by the lifting surface of the baseline blade is approximately $-4\,C_p$ at the 10 m/s inlet velocity and reaches almost $-1\,C_p$ at the 25 m/s inlet velocity. Therefore, the original S809 seems to have generated more drag-based torque than lift-based. This has contributed to the lower performance of the baseline model. Moreover, the maximum negative pressures applied to the lifting surface of the modified blade act mostly near the leading edge in comparison to that of the baseline model. This pointed the lifting force towards the direction of rotation, propagating the moment effects to further increase the resulting torque acting on the rotational axis of the modified turbine model and further increasing the torque generated by it.

3.3. Local Velocities

From a distance of 0.5 m, quantitative color mapping of the local velocity profiles shown in Figures 11–14 appears to be in agreement with the analysis of the pressure distribution results. At 10 m/s inlet speed, the relative velocities over the upper surfaces of both models are very similar. This is not the case over the lower surfaces as the velocity under the modified blade is much less than that under the baseline blade, reaching almost 0 m/s as shown by the near blue shadings in Figure 11b, creating much higher velocity and, thus, pressure differential, but this decreased gradually towards the tip of the blade. Nevertheless, the seagull airfoil performed better near the tip at the 10 m/s inlet velocity, and the velocity differential around the modified blade increased further at the 15 m/s inlet velocity in comparison to that around the baseline blade as illustrated in Figure 12,

as regions of the maximum and the minimum velocities represented in the figure by the red and the blue color shading, respectively, are much wider in the case of the modified blade. Surprisingly, this velocity differential increased significantly in comparison to the velocity differential around the baseline model as the inlet velocity increased to the 20 m/s and 25 m/s inlet velocities in Figures 13 and 14, respectively, even near the tip of the blade.
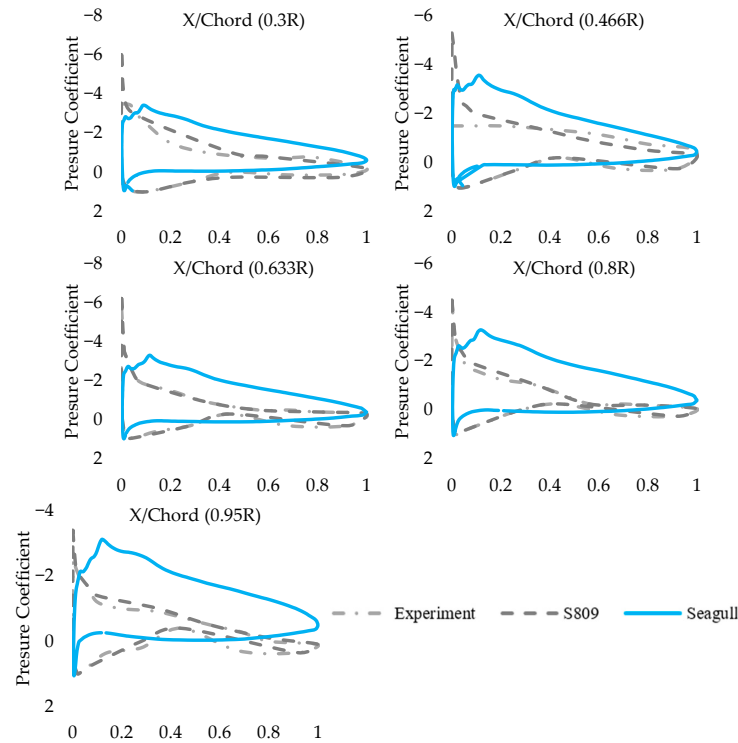
Figure 7. Pressure coefficient at 10 m/s inlet velocity.
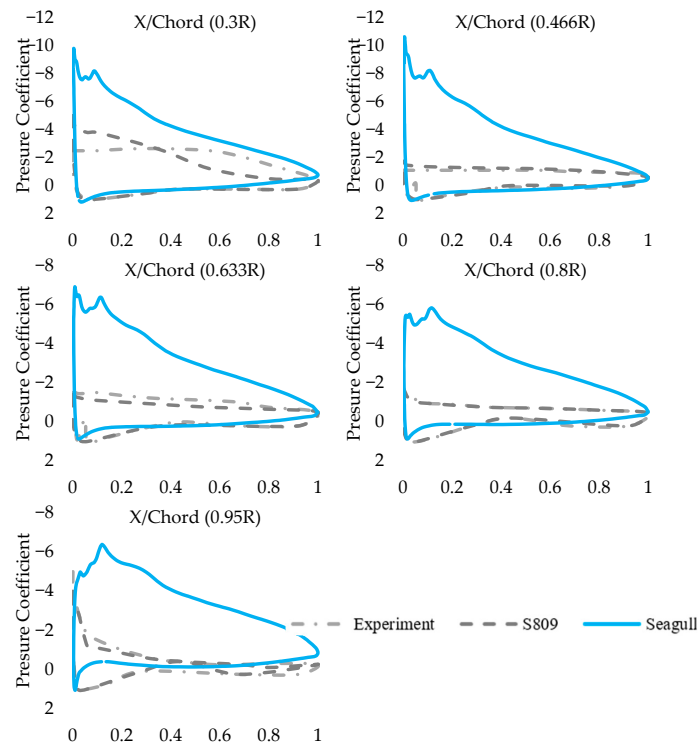
Figure 8. Pressure coefficient at 15 m/s inlet velocity.
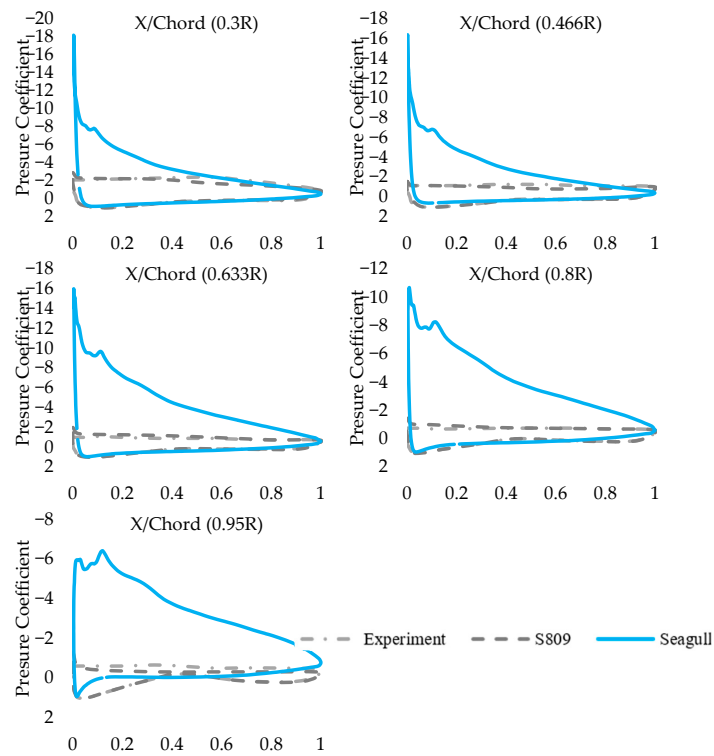
Figure 9. Pressure coefficient at 20 m/s inlet velocity.
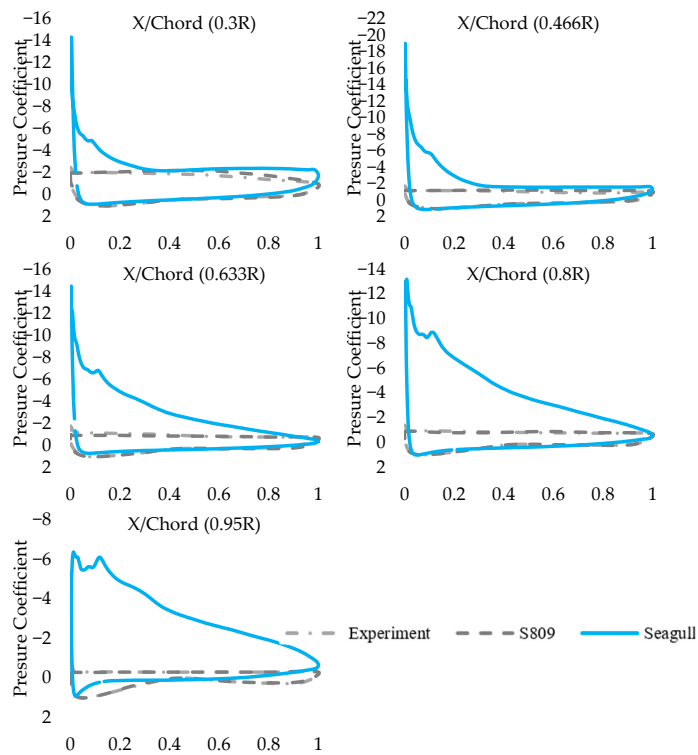
Figure 10. Pressure coefficient at 25 m/s inlet velocity.
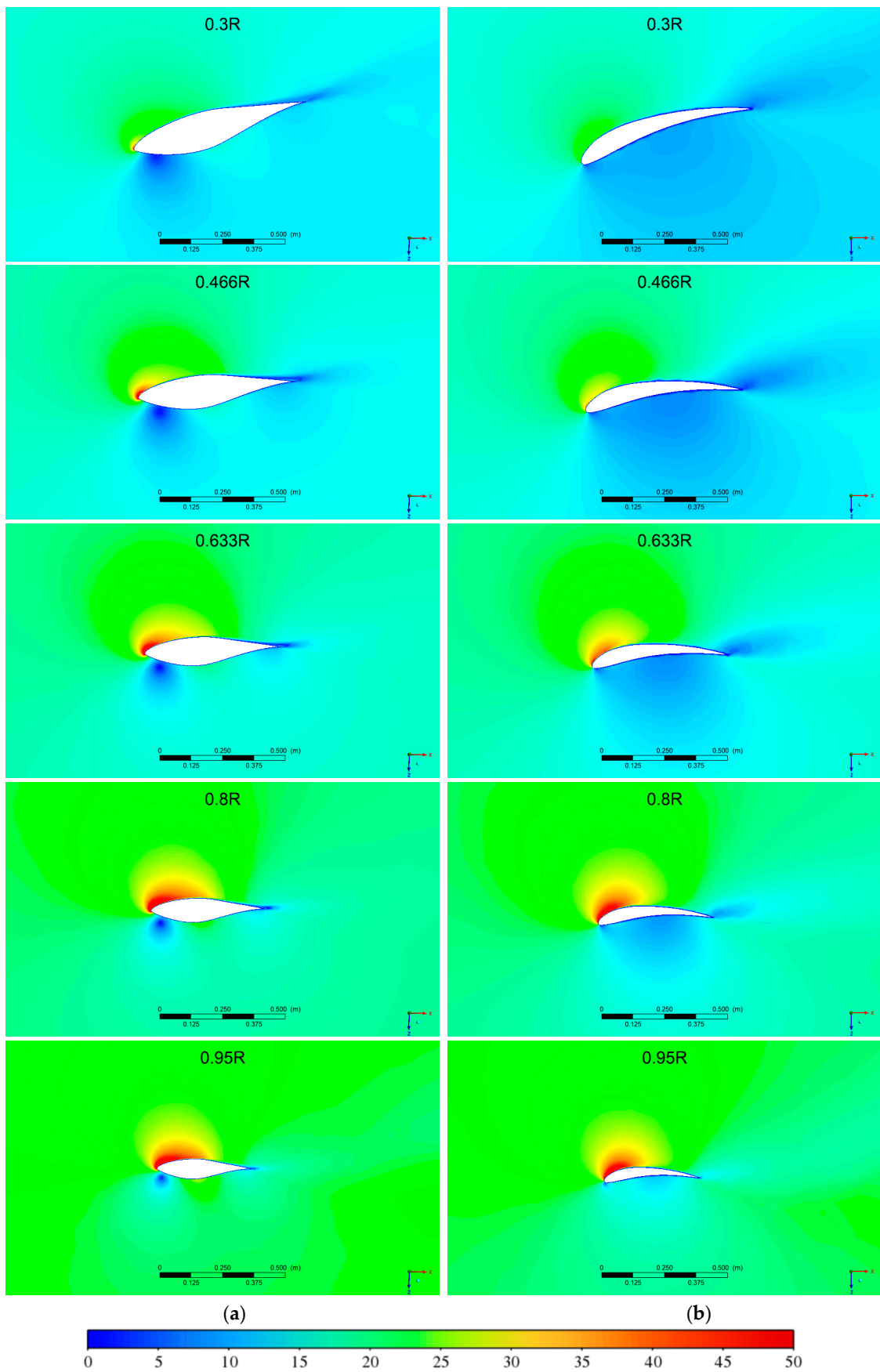
Figure 11. Velocity contours at 10 m/s inlet velocity: (**a**) S809 airfoil, (**b**) modified airfoil.
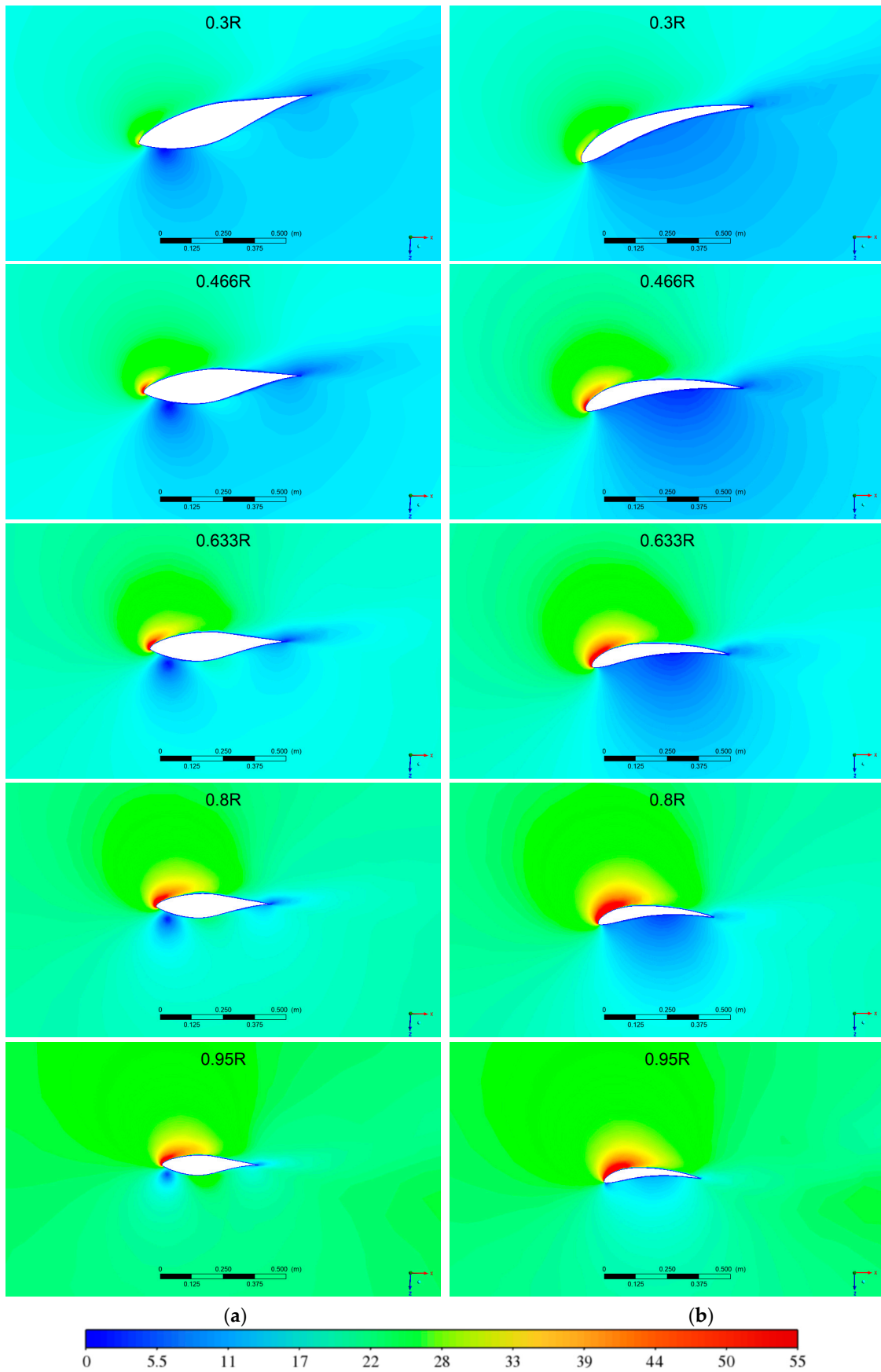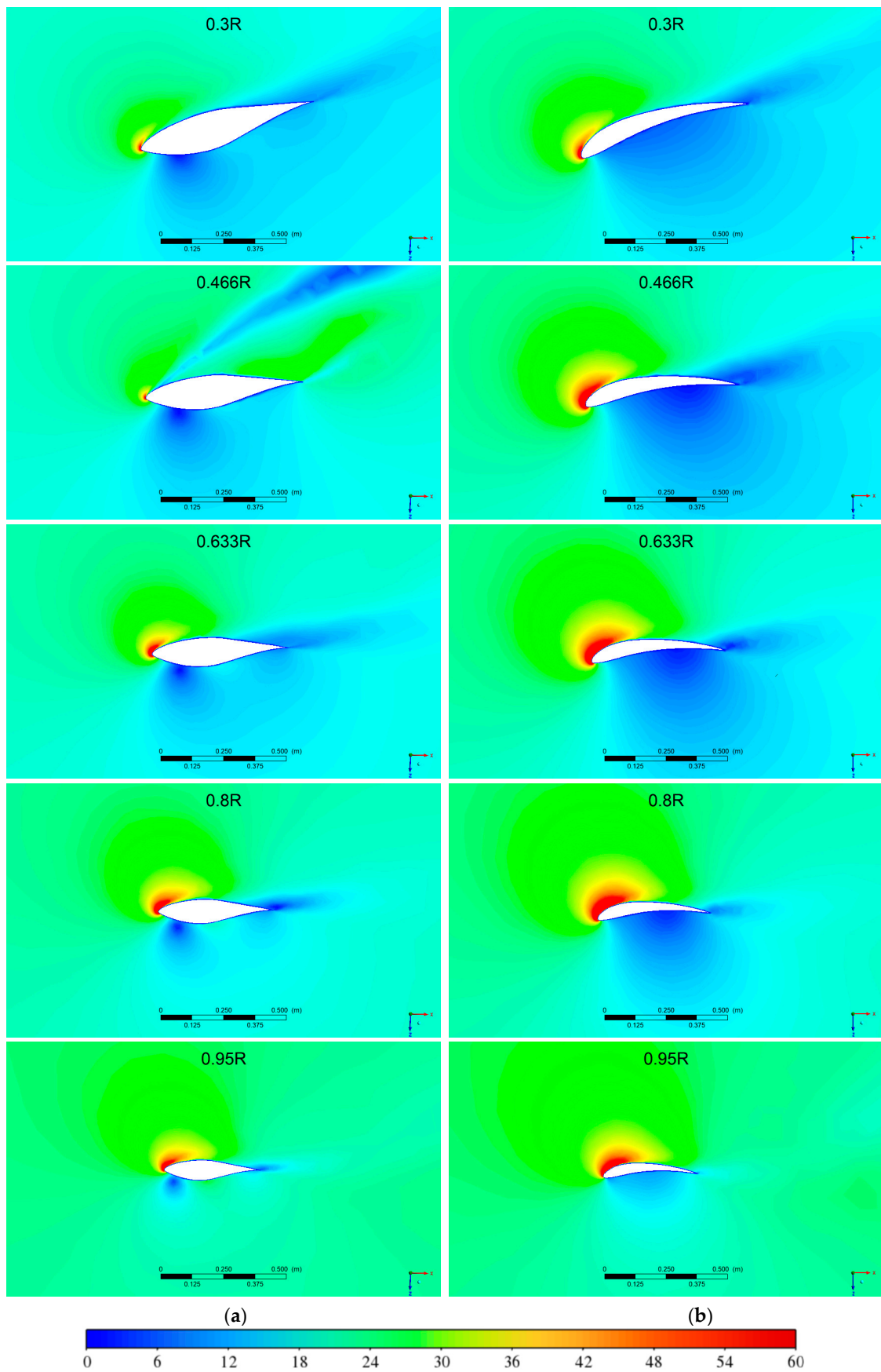
Figure 12. Velocity contours at 15 m/ inlet velocity: (**a**) S809 airfoil, (**b**) modified airfoil.

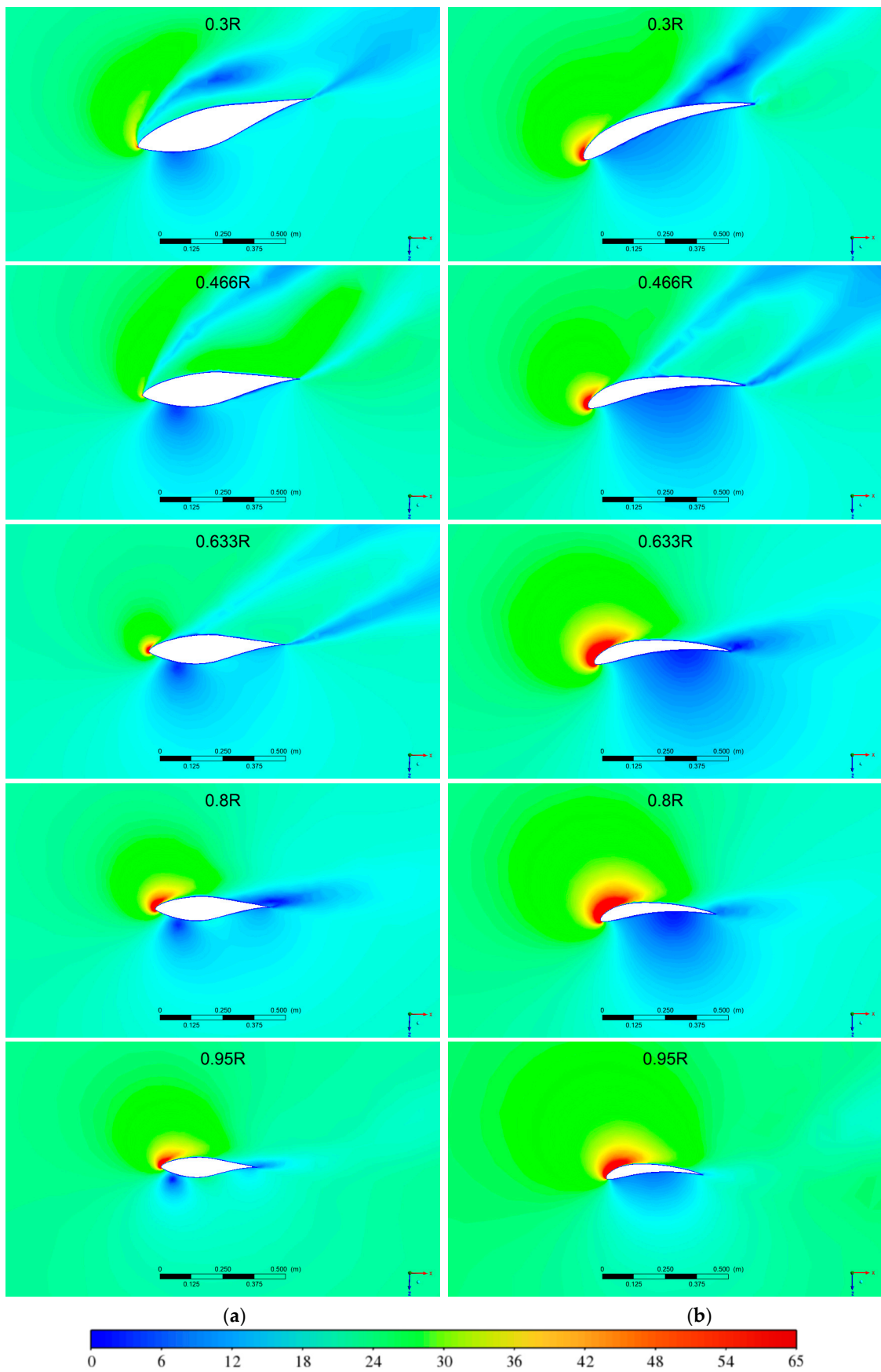**Figure 13.** Velocity contours at 20 m/s inlet velocity: (**a**) S809 airfoil, (**b**) modified airfoil.

Figure 14. Velocity contours at 25 m/s inlet velocity: (**a**) S809 airfoil, (**b**) modified airfoil.

In general, the local velocity profiles confirm the ability of the seagull airfoil profile to modify the velocity profile of the local flow to achieve a highly favorable pressure differential despite the variation in inlet velocity or upcoming wind speed. However, the seagull airfoil profile did not achieve this by increasing the maximum or decreasing the minimum local velocities generated by the S809 airfoil profile, but by increasing the regions of the local maximum and minimum velocity profiles. This contributed to the intensity of the pressure generated by these flow velocities to achieve the considerably high performance achieved by the modified model.

4. Conclusions

This paper investigated the effects of implementing a seagull airfoil profile on the performance of the NREL Phase VI experimental wind turbine. The airfoil profile was obtained by means of three-dimensional laser scanning in a previous work, and the NREL Phase VI wind turbine was selected as the baseline model because of its size and the experimental data it provides, which are necessary for both validation and comparison. The simplicity of the test configuration and conditions of Sequence S of the experiment has helped this research achieve correct results by avoiding incorrect modeling and propagating errors. The results, however, were unexpected as the turbine model implementing the seagull airfoil profile radically outperformed the baseline model even though this profile was not optimized for the operation of the NREL Phase VI wind turbine.

Numerical results from both the baseline and the modified model were compared at five distinguished inlet velocities under the exact same configuration and conditions of the test sequence and validated against the experimental data. An increase in torque output of as high as 823 Nm was achieved at an inlet velocity of 20 m/s by only employing the seagull airfoil in the baseline turbine blades. Considerable increases in torque output of 350, 539, and 577 Nm were also achieved at 10, 15, and 25 m/s inlet velocities, respectively. An analysis and comparison of the pressure distributions and the local velocity profiles around both the baseline and the modified turbine blades revealed that increases in torque outputs are due to the much higher pressure differentials generated by the seagull airfoil profile in comparison to that generated by the baseline model S809 airfoil profile. The analysis also discovered that these higher pressure differentials are not the results of an increase in the values of maximum flow velocity over the lifting surface of the modified blade or the decrease in the minimum values of the flow velocity under this blade but are a result of the ability of the seagull airfoil profile to substantially increase regions of the maximum and minimum flow velocities generated by the baseline blade model. This enabled the seagull airfoil to achieve the favorable pressure differentials that resulted in the considerable improvement in performance that was achieved.

References

1. March, A.I.; Bradley, C.W.; Garcia, E. Aerodynamic Properties of Avian Flight as a Function of Wing Shape. In Proceedings of the ASME International Mechanical Engineering Congress & Expositio, Orlando, FL, USA, 5–11 November 2005.
2. Lees, J.J.; Dimitriadis, G.; Nudds, R.L. The influence of flight style on the aerodynamic properties of avian wings as fixed lifting surfaces. *PeerJ* **2016**, *4*, e2495. [CrossRef] [PubMed]
3. Bourton, J. *Supercharged Swifts Take Flight Speed Record*; BBC News: London, UK, 2010.

4. Grolier. *The New Book of Knowledge*; Scholastic Corporation: New York, NY, USA, 2003; p. 278.

5. Tucker, V.A. Gliding Birds: Reduction of Induced Drag by Wing Tip Slots Between the Primary Feathers. *J. Exp. Biol.* **1993**, *180*, 285–310. [CrossRef]

6. Weimerskirch, H.; Guionnet, T.; Martin, J.; Shaffer, S.; Costa, D. Fast and fuel efficient? Optimal use of wind by flying albatrosses. *Proc. R. Soc. Lond. Ser. B Biol. Sci.* **2000**, *267*, 1869–1874. [CrossRef] [PubMed]

7. Günther Pfeifhofer, H.T. The Flight of Albatross—How to Transform It into Aerodynamic Engineering? *Engineering* **2014**, *6*, 427–438. [CrossRef]

8. Robles, G.E.; Luna, E.C.R.; Tayactac, R.G.; Honra, J.P.; Calderon, A.D. Design and Aerodynamic Analysis of a Bio-inspired HAWT with Albatross and Stork Airfoil for Low Wind Velocity using CFD. In Proceedings of the 6th International Conference on Power and Energy Engineering, Shanghai, China, 25–27 November 2022.

9. Anderson, J.D. *Fundamental of Aerodynamics*; McGraw-Hill: Boston, MA, USA, 2001.

10. Buhl, M. Wind Turbine Airfoil Families. National Renewable Energy Laboratory. 6 July 2012. Available online: https://wind.nrel.gov/airfoils/AirfoilFamilies.html (accessed on 11 July 2021).

11. Yossri, W.; Ayed, S.B.; Abdelkefi, A. Evaluation of the efficiency of bioinspired blade designs for low-speed small-scale wind turbines with the presence of inflow turbulence effects. *Energy* **2023**, *273*, 127210. [CrossRef]

12. Coxworth, B. Seagull-Inspired Blades Could Give Small-Scale Wind Turbines a Power Boost. 24 June 2019. Available online: https://newatlas.com/seagull-wing-wind-turbine-blades/60277/ (accessed on 13 July 2021).

13. Seagull-Wing-Inspired Small-Scaled Wind Turbine to Deliver 15% More Power. 5 July 2019. Available online: https://www.energytrend.com/news/20190705-14345.html (accessed on 13 July 2021).

14. Liu, T.; Kuykendoll, K.; Rhew, R.; Jones, S. Avian Wing Geometry and Kinematics. *AIAA J.* **2016**, *44*, 954–963. [CrossRef]

15. Song, Y.; Perot, J.B. CFD Simulation of the NREL Phase VI Rotor. *Wind Eng.* **2015**, *39*, 299–310. [CrossRef]

16. Yelmule, M.M.; Vsj, E.A. CFD predictions of NREL Phase VI Rotor Experiments in NASA/AMES Wind tunnel. *Int. J. Renew. Energy Res.-IJRER* **2013**, *3*, 261–269.

17. Suárez, J.M.; Doerffer, P.; Szulc, O. *CFD Validated Technique for Prediction of Aerodynamic Characteristics on Horizontal Axis Wind Energy Turbines*; EWEA Offshore: Copenhagen, Denmark, 2015.

18. Elfarra, M.A.; Sezer-Uzol, N.; Akmandor, I.S. NREL VI rotor blade: Numerical investigation and winglet design and optimization using CFD. *Wind Energy* **2014**, *17*, 605–626. [CrossRef]

19. Li, D.; Zhang, Z.; Zhou, X.; Zhang, Z.; Yang, X. Cross-wind dynamic response of concrete-filled double-skin wind turbine towers: Theoretical modelling and experimental investigation. *J. Vib. Control.* **2023**, 10775463231186708. [CrossRef]

20. WebPlotDigitizer. Available online: https://apps.automeris.io/wpd/ (accessed on 15 January 2023).

21. Hand, M.M.; Simms, D.A.; Fingersh, L.J.; Jager, D.W.; Cotrell, J.R.; Schreck, S.; Larwood, S.M. *Unsteady Aerodynamics Experiment Phase VI: Wind Tunnel Test Configurations and Available Data Campaigns*; National Renewable Energy Laboratory: Golden, CO, USA, 2001.

22. Sorensen, N.N.; Michelsen, J.A.; Schreck, S. Navier–Stokes predictions of the NREL phase-VI rotor in the NASA Ames 80ft x 120ft wind tunnel. *Wind Energy* **2002**, *7476*, 151–169. [CrossRef]

23. Johansen, J.; Sørensen, N.N.; Michelsen, J.A.; Schreck, S. Detached-eddy simulation of flow around the NREL Phase VI blade. *Wind Energy* **2002**, *5*, 185–197. [CrossRef]

24. Chao, D.D.; Van Dam, C.P. Computational aerodynamic analysis of a blunt trailing-edge airfoil modification to the NREL Phase VI rotor. *Wind Energy* **2007**, *10*, 529–550. [CrossRef]

25. Hsu, M.C.; Akkerman, I.; Bazilevs, Y. Finite element simulation of wind turbine aerodynamics: Validation study using NREL Phase VI experiment. *Wind Energy* **2014**, *17*, 461–481. [CrossRef]

26. Simms, D.; Schreck, S.; Hand, M.; Fingersh, L.J. *NREL Unsteady Aerodynamics Experiment in the NASA-Ames Wind Tunnel: A Comparison of Predictions to Measurements*; National Renewable Energy Laboratory: Golden, CO, USA, 2001.

27. 40-BY 80-/80-BY 120-Foot Wind Tunnels. NASA Ames Research Center. Available online: https://rotorcraft.arc.nasa.gov/Research/Facilities/windtunnels.html (accessed on 15 January 2023).

28. Sihag, S.; Kumar, M.; Tiwari, A.K. CFD Validation and Aerodynamic Behaviour of NREL Phase VI Wind Turbine. In Proceedings of the International Conference on Materials Science and Engineering, Paris, France, 19–20 October 2022.

29. Betz, A. *Introduction to the Theory of Flow Machines*; Pergamon Press: Oxford, UK, 1966.

30. Burton, T. *Wind Energy Handbook*; John Wiley and Sons: Hoboken, NJ, USA, 2001.